Resonant Acoustic MEMS Wake-Up Switch

Jonathan J. Bernstein, *Senior Member, IEEE*, Mirela G. Bancu, Eugene H. Cook, Amy E. Duwel, Richard D. Elliott, Douglas A. Gauthier, Stephanie L. Golmon, John J. LeBlanc, Michael J. Tomaino-Iannucci, Jonathan S. Ung, and Marc S. Weinberg

***Abstract*— We have designed a novel microelectromechanical systems (MEMS) resonant acoustic wake-up switch which is actuated by ambient sound waves, using zero power while waiting for a signal at its resonant frequency and less than 10 nW when the signal is detected. The system uses a battery to charge a capacitor through MEMS switches activated only by the target signals. The sensor is of rotational design allowing it to be insensitive to linear vibration and static gravity forces. Analysis and experimental results maximizing the Q of these resonators in air are presented. A simple, novel fabrication process is presented which uses silicon-on-insulator bonded wafers and still provides metal–metal electrical contacts. These devices have successfully detected 80-Hz sound as low as 0.005 Pa rms (48-dB SPL // 20 μPa) from a generator. [2017-0282]**

***Index Terms*— MEMS, resonant, microphone, low power, IOT, UGS, switch, relay.**

I. Introduction

LONG term unattended monitoring of physical phenomena is currently based on battery powered sensors and low power electronics which are limited by power consumption to periods of days or weeks. We describe a zero-power acoustic wake-up switch that will enable sensor systems that last for years, limited only by battery self-discharge. The switches are MEMS acoustic devices that intermittently close contacts when excited at their resonant frequencies. The resonant frequencies are designed and tuned to match desired targets. Switches at different frequencies can be combined to perform logic functions such as AND, OR and NOT to listen for combinations of frequencies or reject out-of-band clutter. These devices may be useful for extending battery life of both Internet of Things (IOT) nodes and Unattended Ground Sensors (UGS).

II. Acoustic Switch Design

Most microphones are designed with a low mass/area diaphragm which translates with pressure, to provide wide bandwidth, reduce acceleration sensitivity and avoid sharp resonances [1]. In contrast, this resonant switch is thick (400 μm), has weak torsional springs and a sharp resonance with a Q up to ~300 (free-space resonance in air). Sensitivity to gravity and acceleration is reduced by using a rotational design with pendulosity close to zero. The motivation for selecting a rotational sensor is as follows: For a translational mass-spring-damper system, the "displacement per g" is

$$DPG = \frac{mg}{k_{sp}} = \frac{g}{\omega_0^2} \tag{1}$$

Where m is mass and k_{sp} is the spring constant. For a 60 Hz sensor this is 69 μm/g, which is much larger than our desired sense gap of a few microns. In contrast, a rotational sensor with near zero pendulosity can have near zero displacement due to linear acceleration.

The rotating plate has a solid side which integrates the ambient pressure wave to create a torque, and a perforated side which does not react to the acoustic signal, but reduces pendulosity near zero, shown in Figures 1 and 2. A cavity under the solid side provides acoustic compliance and can be varied to tune the resonant frequency, similar to a Helmholtz resonator. Draper has previously fabricated and patented a rotary microphone [2].

A microphone is a device for transducing pressure into another domain, typically a voltage or current. This switch is not a microphone, it only produces an output when a preselected acoustic frequency surpasses a threshold level. The resonant switch uses a pair of metal-coated contact points (shown in Figs. 2, 3, 9 and 11) rather than an analog capacitive or piezoelectric pickoff. These contact points between the device layer and handle layer of an SOI wafer are metallized by angled evaporation or sputtering.

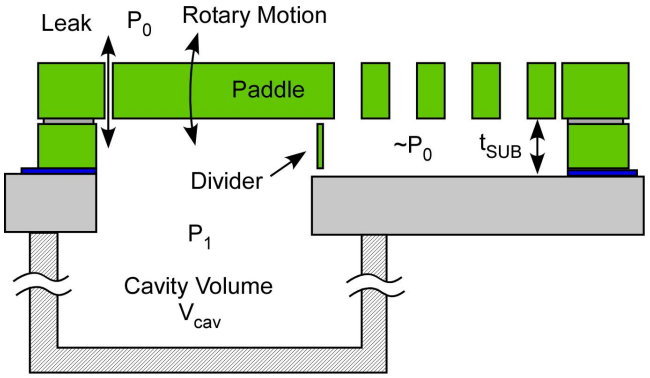

Fig. 1. Cross section of rotational acoustic switch with solid side and perforated side. Leakage path shown at edge of paddle.

Manuscript received November 12, 2017; revised March 22, 2018; accepted April 22, 2018. This work was supported by the DARPA Microsystems Technology Office N-ZERO Program under Contract # HR0011-15-C-0138. Subject Editor G. Piazza. *(Corresponding author: Jonathan J. Bernstein.)*

J. J. Bernstein is with Materials Engineering and Microfabrication, Draper, Cambridge, MA 02139 USA (e-mail: jbernstein@draper.com).

M. G. Bancu, E. H. Cook, A. E. Duwel, R. D. Elliott, S. L. Golmon, J. J. LeBlanc, M. J. Tomaino-Iannucci, J. S. Ung, and M. S. Weinberg are with Draper, Cambridge, MA 02139 USA.

D. A. Gauthier is with Kurt J. Lesker Company, Jefferson Hills, PA 15025 USA.

Color versions of one or more of the figures in this paper are available online at http://ieeexplore.ieee.org.

Digital Object Identifier 10.1109/JMEMS.2018.2830322

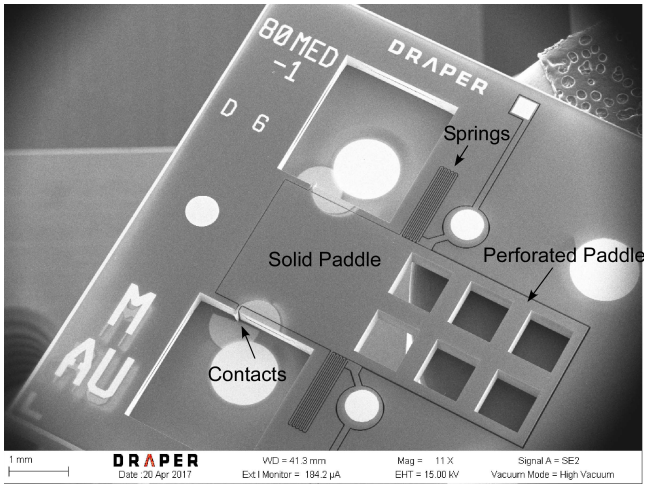

Fig. 2. SEM of Acoustic Switch.

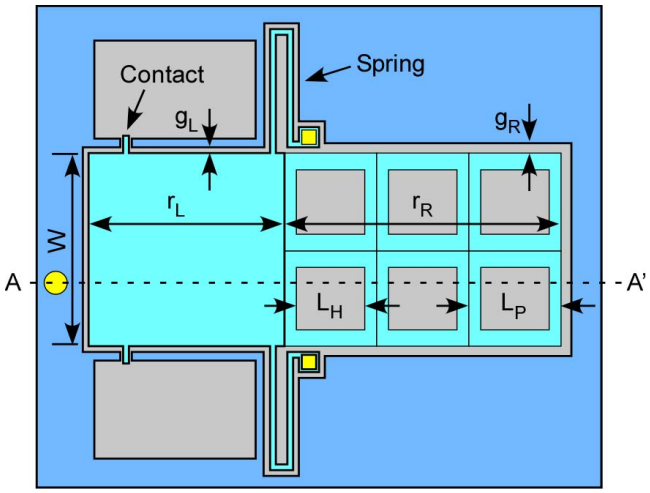

Fig. 3. Diagram defining dimensional variables. Also top-view for cross-sections shown in Fig. 8.

In response to a pressure wave, the solid side sees a differential pressure causing rotation, while the perforated side sees almost the same pressure on both sides. A divider etched from the handle of the SOI wafer separates the cavity under the solid side from the cavity under the perforated side. The pressure drop across the holes is small because of the low resistance to flow through the holes, and because the small cavity under the perforated side represents a high acoustic impedance, limiting flow through the perforations. Damping caused by even this small flow through the holes is significant and is included in the model as part of resistor R_D shown in Figure 4.

Small, Medium and Large devices were designed and built with paddle dimensions given in Table 1. The holes are, by design, 50% of the area of the right side, which is also $\sqrt{2}$ longer to give approximately zero pendulosity. Final dimensions (defined in Fig. 3) are given in Table 2.

Much of the acoustic analysis of the device follows the standard methods given in acoustics textbooks [3], [4] in which voltage is analogous to pressure (Pa) and current is analogous

TABLE I
DIMENSIONS OF ACOUSTIC DEVICE PADDLES

	Small	Medium	Large
Solid Length r_L (mm)	2	2.5	2.5
Width W (mm)	2	2.5	5
Perforated Length r_R (mm)	2.83	3.54	3.54

TABLE II
FINAL PARAMETER VALUES FOR 80 HZ MEDIUM DESIGN

Parameter	Value	Parameter	Value
r_L	2.5 mm	L_P	1.71 mm
r_R	3.54 mm	g_L	15 µm
W	2.5 mm	g_R	30 µm
L_H	1.21 mm	Paddle thickness	400 µm

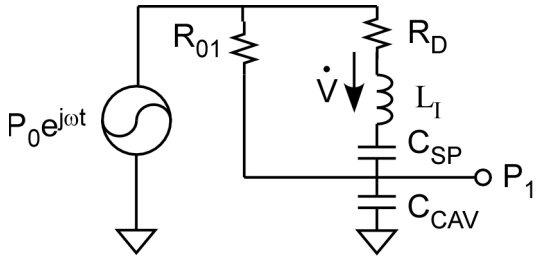

Fig. 4. Acoustic equivalent circuit of device.

to volume flow (m^3/s). Additions to the standard models to accommodate a rotating paddle are derived below.

The device was analyzed using both first principles and an acoustic lumped element equivalent circuit model shown in Figure 4. We will define each of the elements of the equivalent circuit diagram, and then examine the various contributions to damping so that these can be minimized. We derive the equations for a rotational acoustic transducer as follows:

The volume displacement (m^3) through the device per radian of rotation is given by

$$\frac{\Delta V}{\Delta \theta} = \frac{W r_L^2}{2} = \phi \tag{2}$$

where r_L is the maximum extent of the solid (left) side of the paddle (shown in Fig. 3), measured from the axis of rotation, W is the width of the paddle in the orthogonal direction. We define a conversion constant ϕ which is useful for converting between acoustical and rotational quantities.

The torque per Pa of differential pressure across the solid side is derived by integrating the pressure times lever-arm over the face of the solid side, and is also equal to ϕ:

$$\frac{\tau}{Pa} = \phi \tag{3}$$

The acoustic compliance of the cavity (units: m^3/Pa) is given by

$$C_{CAV} = \frac{V_{CAV}}{\gamma P_{atm}} \tag{4}$$

where V_{cav} is the cavity volume, γ is the ratio of isothermal to adiabatic specific heats for air (= 1.4), and P_{atm} is atmospheric

pressure. The resonant frequency is determined by the moment of inertia of the paddle, the torsional spring constant of the silicon springs, and the cavity compliance. We used a variable cavity with a screw-in plunger to vary V_{CAV} and tune the resonant frequency.

$$f_0 = \frac{1}{2\pi}\sqrt{\frac{C_{SP}+C_{CAV}}{L_I C_{SP} C_{CAV}}} \tag{5}$$

The torsional spring stiffness k_θ can be converted to an equivalent acoustic compliance:

$$\boldsymbol{C_{SP} = \frac{\phi}{k_\theta}} \tag{6}$$

For these devices, a large cavity volume leads to a higher Q and therefore higher sensitivity at resonance. To achieve higher Q, cavities as large as 15 cc were used, which was equivalent to a compliance 11.9× greater than the silicon mechanical spring's compliance for an 80 Hz medium device.

The equivalent circuit shown in Figure 4 was modeled using acoustic quantities in which pressure is the analog of voltage, and volume flow $\dot{V}$ is the analog of current. Using the above equations the rotational quantities can easily be transformed into acoustic units. In this diagram, the input pressure wave is P_0, C_{SP} is the acoustic compliance of the torsional spring (the MEMS silicon (physical) springs), L_I is the acoustic representation of the moment of inertia I of the paddle, R_D is the sum of the various viscous damping terms from rotation of the paddle, and R_{01} represents all parallel air leakage paths into the acoustic cavity.

The moment of inertia I can be converted into acoustic units by equating the rotational kinetic energy to an acoustic inductor L_I with acoustic volume flow $\dot{V}$

$$\frac{1}{2}\boldsymbol{I\dot{\theta}^2} = \frac{1}{2}\boldsymbol{L_I\dot{V}^2} \tag{7}$$

Solving for L_I and using equation 2 gives

$$\boldsymbol{L_I = \frac{I}{\phi^2}} \tag{8}$$

The acoustic leakage path around the three edges of the solid side of the paddle is the dominant leakage path (represented by R_{01} in Figure 4). This leak reduces the Q and therefore the sensitivity of the sensor. Assuming viscous flow through the rectangular channel the edge leakage resistance is given by R_{01}.

$$\boldsymbol{R_{01} = \frac{12\mu t_{si}}{g_L^3(W+2r_L)}} \tag{9}$$

where μ is the viscosity of air, t_{Si} is the paddle thickness, g_L is the gap around the paddle on the solid side, and W and r_L are the paddle solid side width and length defined in Fig. 3. To maintain high sensitivity a narrow gap ($g_L = 15\ \mu$m) is used on the solid side and wider gap on the perforated side.

Air damping limits the Q of the device; we have identified five main components:

1) Viscous shear around the edge of the device
2) Air flow through the holes
3) Squeeze-film damping between the solid parts of the perforated side and the package beneath
4) Squeeze-film damping between the contacts and the handle wafer
5) "RC" damping dependent on leakage path R_{01} and cavity volume C_{cav} (Fig. 4)

A narrow gap (15 μm) is necessary around the solid side of the paddle to limit air leakage into the cavity, however to reduce damping the gap around the perforated side is set to be twice as large (30 μm). Resistance to flow through the holes is minimized by using large holes (results shown in Test Results section). Squeeze film damping between the perforated paddle and the package is reduced by moving the sensor away from the package with a spacer chip (0.7 mm thick), increasing the gap t_{sub} shown in Figure 1.

A. Squeeze-Film Damping

Damping between the contacts and the handle wafer can be reduced by minimizing the length and width of the contact arms overlap with the handle layer. Increasing the SOI buried oxide (BOX) thickness t_{BOX} also reduces this squeeze film damping (proportional to $1/t_{BOX}^3$), although there are other tradeoffs with increasing BOX thickness since a larger angular motion (proportional to t_{BOX}) is required to make contact.

B. RC Damping

This damping only appears in a packaged device with an acoustic back cavity. Motion of the paddle creates a volume flow $\dot{V}$ into the cavity, which creates a pressure P_1 in the cavity. This pressure induces flow through the leakage resistance R_{01} in the equivalent circuit, which is an energy loss and limits Q. Assuming sinusoidal motion of the paddle, we can solve for the pressure in the cavity, and then calculate the average energy loss in R_{01}. Using the definition of Q as $2\pi^*$ (*energy stored/energy lost/cycle*) we can derive Q_{RC} as:

$$Q_{RC} = L_I C_{CAV}^2 \omega_0^3 R_{01} \tag{10}$$

For the un-packaged chips Q as high as 300 was observed. Once packaged, the RC damping becomes dominant, with Q typically 50 to 100 depending on the cavity volume.

C. Edge Damping

Motion of the paddle causes viscous shear losses around the periphery of the paddle. The viscous force/area is given by $F_v = \mu v/gap$ where μ is the gas viscosity, v is the relative velocity of the two surfaces and *gap* is the gap between the moving paddle and the stationary silicon surrounding it [5]. To convert from linear damping to rotational damping (torque/angular-velocity) we integrate this force around the entire perimeter, multiplying by the distance to the rotation axis squared. As shown in Fig. 3, the perforated (left) and solid (right) sides have two different gaps g_R and g_L and two different lengths r_R and r_L, W is the width of the paddle and t_{Si} is the thickness. The edge rotational damping is:

$$\boldsymbol{\frac{\tau_{edge}}{\dot{\theta}} = \frac{2t_{si}\mu}{3}\left[\frac{r_R^3}{g_R}+\frac{r_L^3}{g_L}\right] + Wt_{si}\mu\left[\frac{r_R^2}{g_R}+\frac{r_L^2}{g_L}\right]} \tag{11}$$

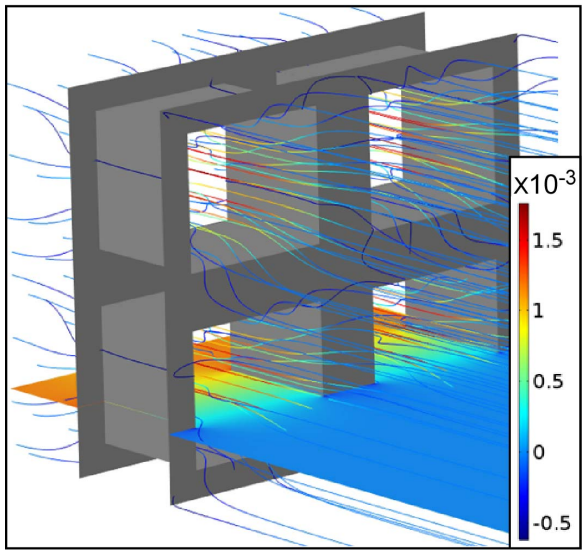

Fig. 5. FEA showing flow-lines through an array of holes. Pressure drop (Pa) is shown in bottom plane.

D. Hole Damping

Resistance to air flow through the square holes can be approximately modeled as Poiseuille flow neglecting entrance and exit effects. For a single square hole with edge size L_h, the flow resistance (Pa-s/m^3) can be derived using the equivalent radius of a square hole [6]

$$R_{hole} \approx \frac{28.5\mu t_{si}}{L_h^4} \tag{12}$$

where we have used the equivalent radius R_{hole} (= diameter d_e /2) of a square hole of side length L_h: $d_e = 1.093L_h$. Assuming all the air from hole unit cell of area L_p^2 flows through the hole, and integrating the torque over the perforated side of the paddle, the holes rotational damping is given approximately by

$$\frac{\tau_{holes}}{\dot{\theta}} = 9.5W\mu t_{si}\left(\frac{L_p^2}{L_h^4}\right)r_R^3 \tag{13}$$

FEA software was used to simulate both air flow through the perforated side and squeeze film damping between the paddle and the package. Figure 5 shows a COMSOL™simulation of flow lines and pressure drop for a perforated paddle in linear motion. The left boundary represents the package under the paddle, while the right boundary is free. The simulation shows that the pressure drop is primarily in the hole region, while the flow lines indicate that the flow redistributes perpendicular to the primary flow axis at the entrance and exit of the holes. This lateral flow contributes to squeeze film damping, which is an important damping component.

Fig. 6 compares equation 12 for flow through a square channel with FEA results which include both hole resistance and squeeze-film effects between the paddle and a substrate. At small hole sizes, the hole damping dominates but at larger hole sizes, squeeze film damping dominates and the difference between equation 12 (hole resistance only) and the FEA results gets larger.

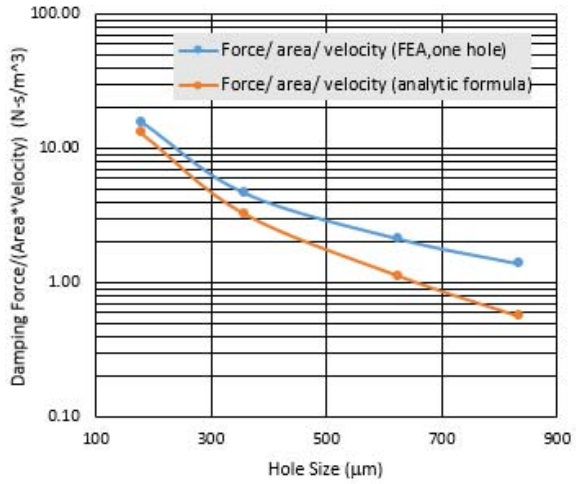

Fig. 6. Comparison of analytical single-hole damping formula with FEA hole + squeeze-film damping vs. hole size.

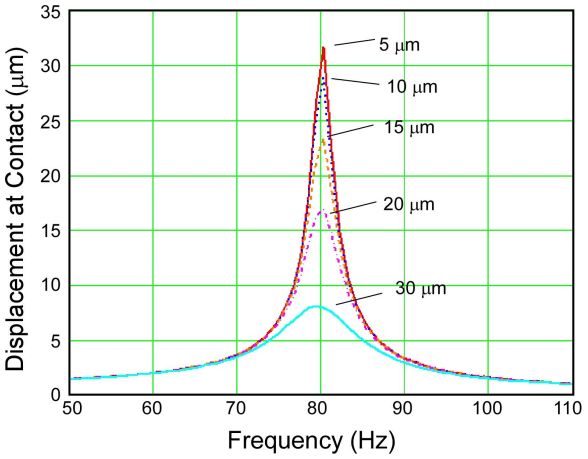

Fig. 7. Calculated effect of slot width (5-30 μm) around 3 edges of the solid side of the paddle based on circuit model of Fig. 4. Air leakage R_{01} reduces sensitivity and Q.

The model based on the equivalent circuit in Fig. 4 was used to calculate the displacement in μm/Pa of the paddle at the contact versus frequency with the perimeter gap g_L as a parameter. Figure 7 shows the strong effect of the edge gap and RC damping on the response and Q. The width of this edge gap g_L is limited to about 15-20 μm $\times$ 400μm deep (the paddle thickness) based on current plasma etching technology. In this calculation for an 80 Hz medium device, $L_I = 4.82 \times 10^5$ kg-m^{-4}, and $C_{CAV} = 2.14 \times 10^{-11}$ m^3/Pa, corresponding to a 3 cc cavity.

III. Fabrication

The fabrication starts with 150 mm diameter silicon-on-insulator (SOI) wafers: 400 μm device layer, 2 or 4 μm buried oxide (BOX) and 300 μm handle. The first step (Fig. 8a) is a Cr/Pt/Au metal liftoff for bondpads and alignment marks. The second step is the front inductively coupled plasma (ICP) etch, shown in Fig. 8b. Following that is the back ICP etch, shown in Fig. 8c. After dicing and cleaning the wafer, the die are released in vapor HF, shown in Fig. 8d.

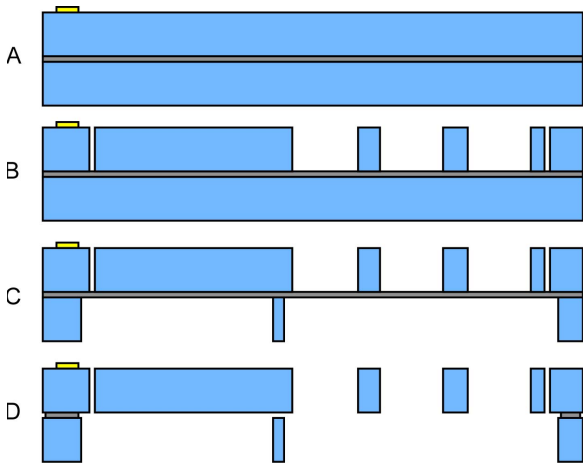

Fig. 8. Cross-sectional views of device fabrication. (a) Lift-off bondpad metal. (b) Front ICP etch. (c) Back ICP etch. (d) Vapor HF release. Corresponding top view in Fig. 3.

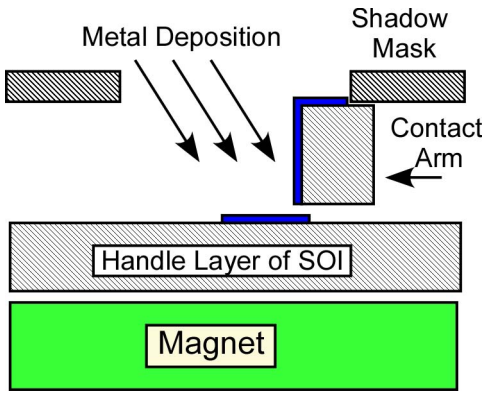

Fig. 9. Angled deposition (through shadow mask) was used to deposit metal contacts between paddle and substrate wafer.

To prevent air leakage under the paddle from the perforated side to the solid side, a divider or partition bar is formed under the axis of rotation during the back ICP etch.

The contact arms are short stubs attached to the solid side of the paddle, which make contact to the handle wafer when acoustic induced displacement equals the sacrificial BOX layer thickness. Metal (typically a Cr/Pt stack, 0.5 to 1 μm total thickness) was deposited on the contacts by sputtering or evaporation through a shadow mask at a 45° angle at the die level (after dicing). The metal deposition in the contact region is sketched in Fig. 9.

Each chip is held in a stack consisting of angle fixture, magnet, sensor chip, and Invar shadow mask. A 150 mm diameter substrate with an array of 45° angle fixtures is shown in Fig. 10.

Figure 11 shows a contact region after metal evaporation. Evaporation is essentially line-of-sight and gave unreliable yield, due to shadowing of the metal under the contacts. It was found that sputtered metal gave higher yield due to the greater angular distribution of the metal deposition, and ability to penetrate under the contact stubs.

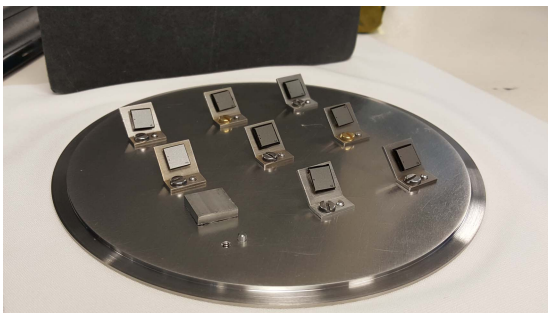

Fig. 10. Angled metallization fixture showing 8 devices covered with shadow masks, held in place by magnets under the sensor chips.

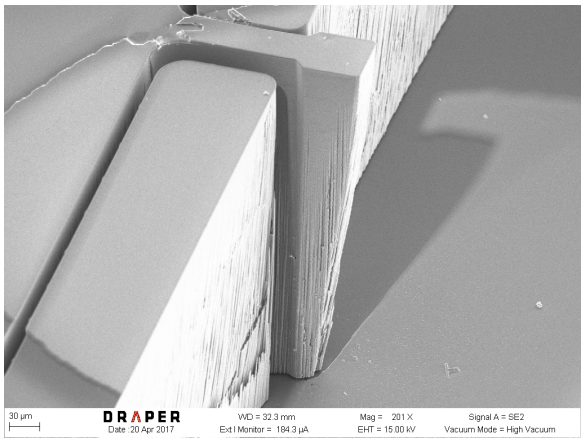

Fig. 11. Contact region after shadow masked evaporation of Cr/Au/Pt at 45° angle. Note shadowing of metal deposition.

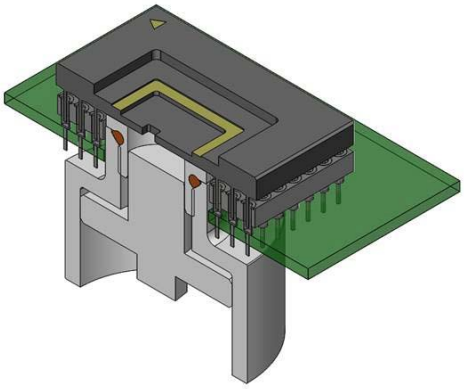

Fig. 12. Cross-section of a solid model of the package and cavity. Frequency adjusting back cavity for acoustic sensor has volume up to 15 cm^3. Plunger screws into cavity creating a variable Helmholtz cavity.

IV. Packaging

The devices are epoxied into pin-grid array packages with through holes formed by laser drilling, shown in Fig. 12. The through hole connects to an acoustic chamber with a variable volume set by a screw-in plunger. By adjusting the cavity volume, the resonant frequency can be fine-tuned to hit the desired frequency with 0.1 Hz accuracy. The ability to tune the frequency post-fabrication is important because minor variations in flexure width can cause several Hz variation in resonant frequency.

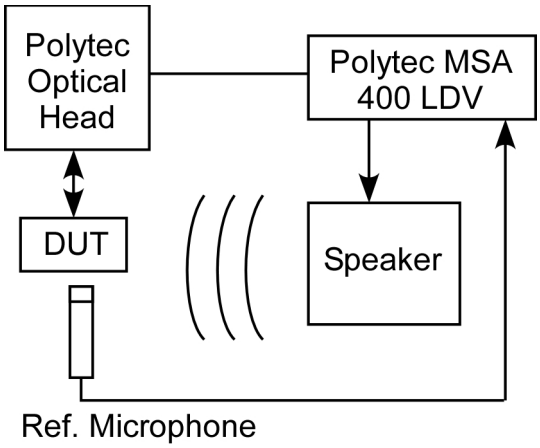

Fig. 13. Test set-up with reference microphone and Polytec MSA 400 Laser Doppler Vibrometer.

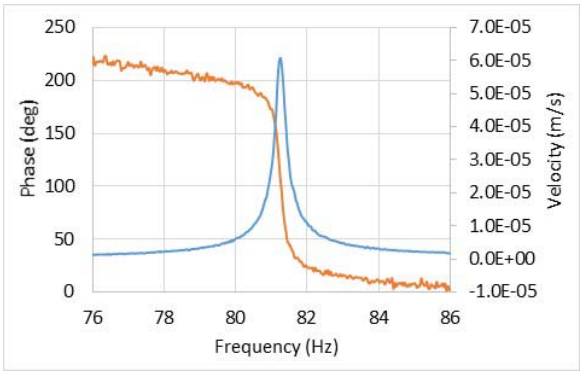

Fig. 14. Frequency response at resonance of "Large" device G8 in air. Q is 323 without "RC" or squeeze film damping.

V. Results

Much of the chip-level testing is carried out with a Laser Doppler Vibrometer, which can directly read out paddle velocity under acoustic excitation from an adjacent speaker. We tested bare die as well as packaged die with acoustic cavities with the setup shown in Figure 13. The low frequency of the measurements (typically < 100 Hz) implies that the sound level measured by the microphone accurately represents the pressure seen by the nearby device. Electrical testing of the contacts was carried out with a 1 V bias across the device under acoustic excitation.

Figure 14 shows a resonance captured by the Polytec LDV on a chip before packaging. The resonant frequency is 81.25 Hz, with a Q of 323 and no "RC" or other package-induced damping factors. Once the package and acoustic cavity are added, RC damping dominates and reduces the Q to typically < 100.

A. Frequency Tuning

A medium size device with a free-space frequency of 62.7 Hz and free-space Q of 92 was packaged and attached to a variable cavity with a maximum volume of 5.7 cm^3 (slightly larger than a sugar cube). The Helmholtz cavity was used to tune the resonant frequency up to 80 Hz. The curves of frequency and Q vs. cavity volume are shown in Fig. 15. The

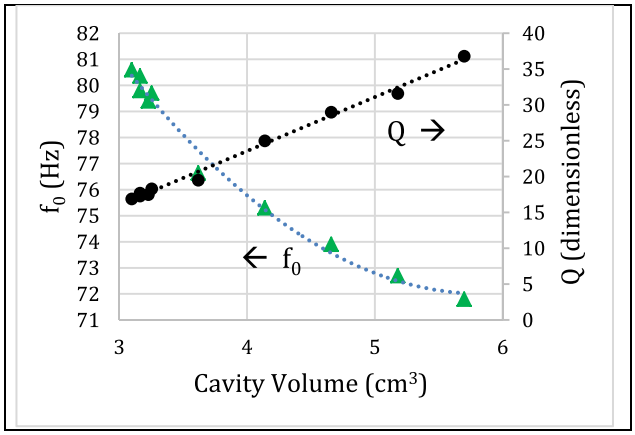

Fig. 15. Measured frequency and Q vs. cavity volume for a medium device with small (5.7 cc maximum) cavity. Frequency decreases and Q increases as volume is increased.

RC damping ($Q_{RC} = 65$) is dominant, reducing the packaged device Q from the free-space value 92 down to 38. From equation 10, it is clear that a large cavity volume maximizes the achievable Q. Larger cavities with volume up to 15 cc were introduced later in the program to increase Q.

B. Effect of Hole Size and Gap on Q

To examine experimentally the effect of varying hole size on Q, a set of devices (called Pathfinder chips) was fabricated with no handle wafer (just the paddle layer, a double side polished wafer) and with hole size on the perforated side varying from 180 μm to 880 μm. A test fixture with large internal volume which holds the chips by the edges with several gaps t_{sub} under the perforated side was constructed. Using these chips and the varying gap fixture, Q was measured with the Polytec LDV as a function of hole size and gap t_{sub}. As expected, the Q increased for the devices with larger hole size and larger gap.

The squeeze-film gap t_{sub} was either 0.3 mm, 0.8 mm or "large", representing either the handle layer of the SOI wafer only, handle wafer plus an additional spacer chip, or a free-space measurement with no nearby surface to cause squeeze film damping. The curves of Q vs. hole size with 3 different squeeze-film gaps are labeled as Q_0.3, Q_0.8, and Q_∞ in Figure 16. Q's of over 300 were measured in the absence of squeeze film damping and with the larger hole sizes. Q's over 200 were measured with a 0.8 mm gap. These Q values do not include the package related RC damping from leakage resistance R_{01} and the cavity volume C_{cav}. Once packaged, the device Q's were reduced to typically < 100 due to squeeze film damping and the RC damping, which was dominant.

C. System Operation

Multiple sensors can be used to detect multiple target frequencies or other types of signals (i.e. vibration or magnetic signals). Highly selective resonant sensors offer one level of discrimination, false positives from clutter may be further rejected by passive logic that drains charge from integration

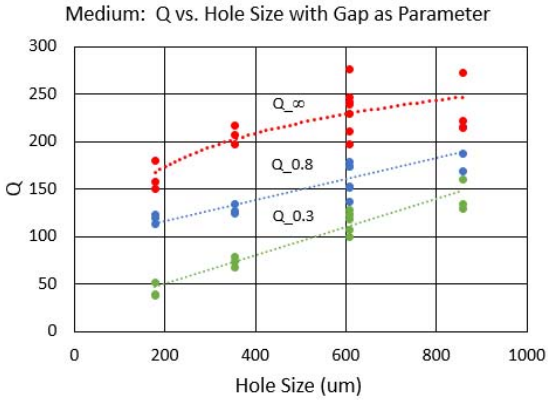

Fig. 16. Q vs. hole size with gap t_{sub} as a parameter shows effect of hole size and squeeze film damping with varying gap. Experimental data from Pathfinder chips and no acoustic cavity.

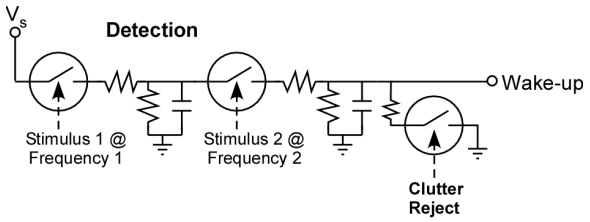

Fig. 17. Circuit diagram for system with two-frequency sensing. Resistors and capacitors are used to limit current flow, implementing AND function requiring presence of multiple frequencies to reduce false alarm rate. Clutter reject sensor can further reduce false alarms.

capacitors. Figure 17 shows a system-level circuit for multiple sensors. This low power switching logic will be used as a preliminary screening to wake-up a higher power system with more signal processing power.

Leakage current through the device in the off state is extremely low, leading to off-state power consumption typically < 1 nW.

The switches are tuned to resonate at a frequency that is indicative of the target. Although the contacts are intermittent, the DC voltage supply (which consumes virtually no power ($<$ 1nW) when the contacts are open), charges up the RC network over a desired time constant to decide if a target is present. Known clutter frequencies can be used to reject undesired signals or broadband noise.

For a demonstration system, an 80 Hz sensor was used to detect a gas-powered portable electric generator, a 65 Hz sensor was used to detect a Ford F150 truck, and a 75 Hz sensor was used as clutter reject.

A sensor resonant at 80 Hz was tested with a recorded acoustic signal from a Honda generator with strong tonal content at harmonics of 20 Hz. Figure 18 shows 3 periods of detection with the generator acoustic signal turned on and off 3 times. The upper trace shows a spectrogram of the reference microphone signal, with streaks at 80 Hz indicating the generator with an average amplitude of 95 mPa (73.5 dB SPL). Out of band acoustic interferers are present at 200-250 seconds. The middle trace shows the integration capacitor voltage charging up over time while the generator signal is played, then discharging. The resonant device does not react much to the out-of-band interferers. The small

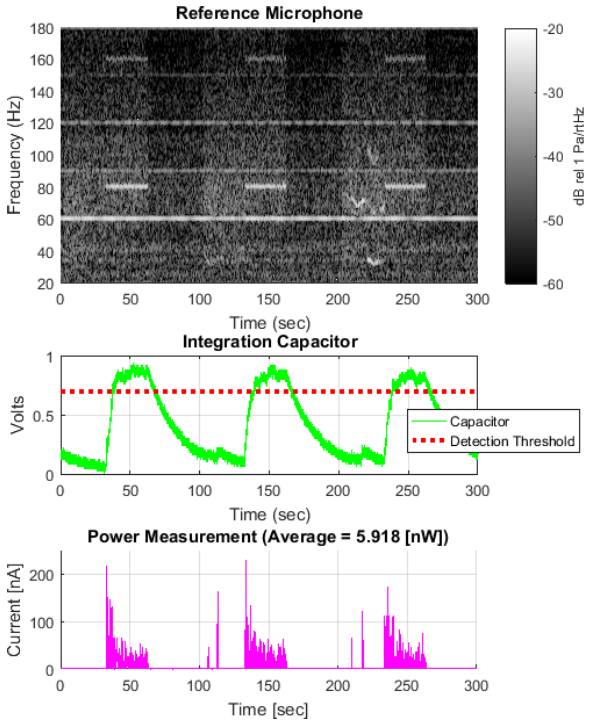

Fig. 18. Three cycles of detection of 80 Hz signal showing a spectrogram of the acoustic signal (upper trace), integration capacitor voltage and threshold (middle trace), and current pulses at contact (lower trace). The out-of-band interferers at 200-250 seconds hardly excite the 80 Hz resonant device.

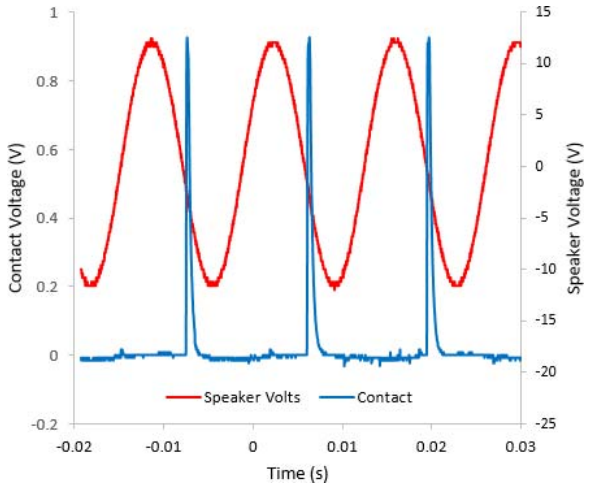

Fig. 19. Upper trace is voltage driving a loudspeaker producing acoustic signal at 73 Hz. Lower trace shows voltage pulses through the contacts displaying one contact per cycle.

voltage that does accumulate while exposed to the interferer does not reach the detection threshold and is discharged over time.

The lower trace shows current spikes through the sensor during signal detection. A one-volt source was used to supply the current. Average power consumption when the generator signal is present was 5.9 nW, and $<$ 1 nW when the signal is not present.

Figure 19 is a recording at higher time resolution showing individual voltage spikes into a load resistor with a 73 Hz acoustic signal. No integration capacitor was used while collecting this data, thus the contact voltage does not

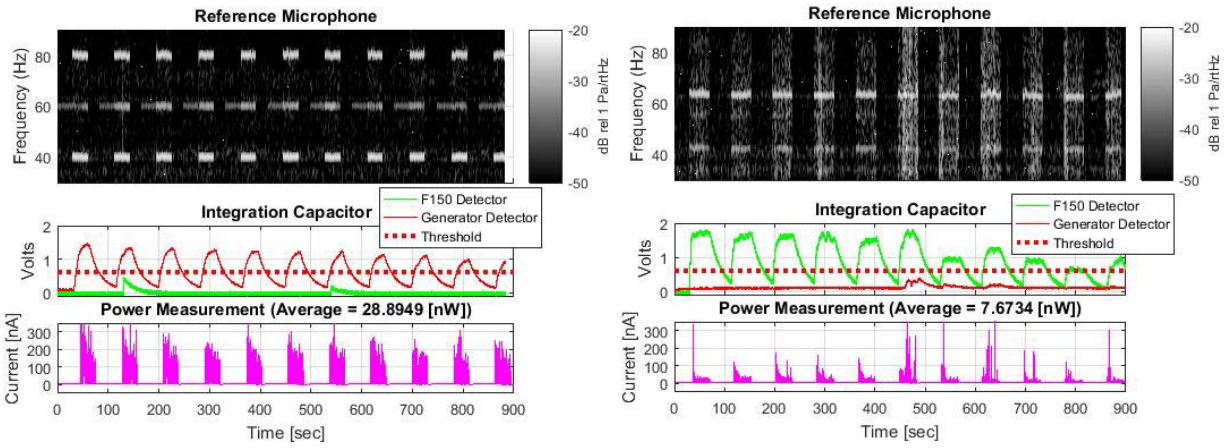

Fig. 20. (a) Performance of an 80 Hz detector for a gas-powered generator and (b) a 65 Hz F150 truck detector circuit. Only the F150 detector crosses the detection threshold when the F150 recording is being played. Similar performance is observed for the 80 Hz generator detector; eleven out of eleven detections with no false alarms.

accumulate. As expected, there is one voltage spike per cycle. Detection has been measured with acoustic signals as low as 0.005 Pa RMS (48 dB SPL) with a sensor tuned to 80 Hz.

Target discrimination was demonstrated by playing recorded acoustic data of an F150 truck and a Honda generator through a loudspeaker in a calibrated test setup. A 65 Hz resonant device was used to detect the F150, while an 80 Hz device was used for the generator detection. Figure 20 shows that the F150 detector charged to the threshold voltage when the F150 recording was played, while the generator detector circuit did not charge significantly. The average power consumed during F150 detection was 7.7 nW. Similarly, the generator detector charged to the threshold voltage when the generator recording was played, while the F150 detector circuit did not charge significantly. The background acoustic environment was typical for indoor lab/office, and included voices and occasionally small equipment turning on/off. The system worked well with 11out of 11 detections for both targets and no false alarms. Both devices consumed $<$ 1nW power in the absence of a signal at their detection frequencies.

VI. Conclusions

Responding to sound inputs, a novel, very low power rotational resonant MEMS acoustic switch has been designed and demonstrated. No power ($<$ 1nW) is consumed until the target frequency is detected. Low frequency, novel acoustic switches have demonstrated high sensitivity with switch closure at pressures as low as 0.005 Pa rms (48 dB SPL // 20 μPa). A generator with frequency harmonics at multiples of 20 Hz was detected successfully at 80 Hz and a truck was detected using a 65 Hz sensor while demonstrating average power consumption of $<$ 1 nW in the absence of the signal. Tuning the acoustic switches by adjusting the volume of a back cavity (similar to a Helmholtz resonator) has been demonstrated to compensate for fabrication tolerances.

Acknowledgment

The excellent work of Joseph Aghia, Dan Reilly, Perri Lomberg, Jason Danis and many other supporting engineers, technicians, and students is gratefully acknowledged. The expert assistance of Karen Gettings of the MIT Lincoln Laboratory with setup and data collection during field trials is also gratefully acknowledged.

The views, opinions, and/or findings expressed are those of the authors and should not be interpreted as representing the official views or policies of the Department of Defense or the U.S. Government.

References

[1] A. J. Sprenkels and P. Bergveld, "The use of silicon technology for an electret microphone construction," in *Proc. 6th Int. Symp. Electrets (ISE)*, Sep. 1988, pp. 593–597.
[2] J. J. Bernstein, "Acoustic transducer," U.S. Patent 5 146 435, Sep. 1, 1992.
[3] J. Merhaut, *Theory of Electroacoustics*. New York, NY, USA: McGraw-Hill, 1981, pp. 32–50.
[4] L. Kinsler, A. Frey, A. Coppens, and J. Sanders, *Fundamentals of Acoustics*, 3rd ed. New York, NY, USA: Wiley, 1982, pp. 231–233.
[5] R. Bird, W. Stewart, and E. Lightfoot, *Transport Phenomena*. New York, NY, USA: Wiley, 1960, p. 4.
[6] R. G. Huebscher, "Friction equivalents for round, square and rectangular ducts," *ASHVE Trans.*, vol. 54, pp. 101–118, 1948.

Jonathan J. Bernstein received the B.S. degree in electrical engineering and physics from Princeton University, and the M.S. and Ph.D. degrees in EECS from the University of California at Berkeley, supported by NSF and Hertz Foundation graduate fellowships. He is with Draper, where he developed micro-electromechanical systems (MEMS) inertial sensors, such as the tuning fork gyro, accelerometers for combined GPS/inertial projects, and seismic sensors. He also developed MEMS hydrophones and microphones for acoustic and ultrasonic detection and solid state ion-conducting atom sources. From 2000 to 2003, he was the Vice President of technology with Corning IntelliSense Corporation, where he led the development of optical, RF, and other MEMS devices, such as two-axis electromagnetic mirror arrays for optical switching, dynamic spectral equalization, and wavelength selective switches. He has authored or co-authored 65 papers and holds over 50 issued patents. He was a recipient of the Motorola Engineering Excellence Award, the Draper Laboratory Distinguished Performance Award, the Draper Lab Annual Award for Best Technical Patent in 1992 and 1994, the Draper Lab Engineering Vice President's Annual Award for Best Publication in 1993, 2011, 2013, and 2017, and the Corning Certificate of Recognition for outstanding efforts and critical contributions to the optical switch program.

Mirela G. Bancu received the M.S. degree in chemical engineering from University "Politechnica," Bucharest, Romania, in 1995, and the M.S. degree in mechanical engineering from Boston University, Boston, MA, USA, in 1999.

From 1999 to 2003, she was a Senior Microelectromechanical Systems (MEMS) Process Engineer with Corning IntelliSense Corporation. In 2004, she joined the Draper Laboratory, where she is currently a Principal Member of the Technical Staff with the Fabrication Processes Group.

She has led and contributed to the MEMS process development and fabrication for numerous MEMS devices, including pendulous integrating gyroscopic accelerometers, microscale rate integrating gyros, tuning fork gyros, acoustic and magnetic sensors, microfluidic devices, LC resonators, ultra-high density packaging, steering mirrors, pressure sensors, and electrospray ionization nozzles.

Eugene H. Cook received the B.S. degree in aerospace engineering from the University of Maryland, College Park, MD, USA, in 2006, and the M.S. and Ph.D. degrees from the Massachusetts Institute of Technology in 2008 and 2011, respectively. He was a Draper Laboratory Fellow with Draper from 2006 to 2011. He holds four patents, with six pending. His research in microelectromechanical systems includes inertial sensors and resonators, micro-optical systems, microswitches, advanced materials including carbon nanotubes, diamond, and silicon carbide, and biodevices including biomimetic adhesives and neural probes. He was a recipient of the Draper Best Paper Award in 2013.

Amy E. Duwel received the B.A. degree in physics from Johns Hopkins University in 1993, and the M.S. and Ph.D. degrees in electrical engineering and computer science from the Massachusetts Institute of Technology in 1995 and 1999, respectively. She led the Microelectromechanical Systems (MEMS) Group and was the Group Leader of the Draper Laboratory's RF and Communications Group. She is currently the Director of the Materials Engineering and Microfabrication Directorate, Draper. She has expertise in materials, MEMS, and RF systems, with special emphasis on energy loss mechanisms and energy transport.

Richard D. Elliott received the B.S. degree in electrical engineering from Boston University, Boston, MA, USA, and the M.S. degree in electrical engineering from Northeastern University, Boston, MA, USA. He has over 25 years of research and development engineering experience delivering first of a kind precision instrumentation and measurement solutions including electromechanical, microelectromechanical systems and optical gyroscopes, accelerometers, magnetometers, and various other transducers, actuators, and systems. He is currently a Distinguished Member of the Technical Staff with Draper. He holds several patents. His diverse background includes expertise in analog and digital signal processing, mixed-signal application-specified integrated circuit and discrete electronics architecture and circuit design, data acquisition and analysis, transducer and actuator physics and design, instrument, modeling, and verification. He was a recipient of the Draper Distinguished Performance Award twice and the Draper Mentor Award.

Douglas A. Gauthier received the B.S. degree in mechanical engineering from the University of Washington, Seattle, WA, USA, in 2006, and the M.S. degree in mechanical engineering from Tufts University, Medford, MA, USA, in 2008. From 2008 to 2017, he was a Senior Member of the Technical Staff with the Charles Stark Draper Laboratory. Since 2017, he has been a Senior Mechanical Engineer with the Kurt J. Lesker Company, Jefferson Hills, PA, USA. His research interests include low power, microscale sensors, alkali-vapor-based optical devices, and advanced electronic packaging.

Stephanie L. Golmon received the B.S. degree in physics and mathematics from the Principia College and the M.S. and Ph.D. degrees in aerospace engineering sciences from the University of Colorado Boulder (CU). She was an NSF Graduate Fellow with CU. At CU, her dissertation work applied multiscale, multiphysics finite-element analysis to lithium-ion batteries to simulate and optimize coupled electrochemical–mechanical phenomena. She was an Applications Engineer with a finite-element software company and also with a start-up focusing on the commercialization of grid-scale liquid metal battery technology. Since 2016, she has been with Draper, performing mechanical design and multiphysics coupled analysis for multiple early-stage research and development programs. She is currently an Engineer and a Scientist with the Mechanical Design and Analysis Group, Draper Laboratory.

John J. LeBlanc received the B.S. degree in physics from Tufts University in 1983 and the M.S. degree in physics from the University of Massachusetts–Lowell in 1985. From 1985 to 2001, he was with Northrop Corporation, first in the Integrated Optics Research Group and then in the Microelectromechanical Systems (MEMS) Research Group, developing gyroscopes and accelerometers. In 2002, he joined the Charles Stark Draper Laboratory, where he has remained with the exception of short excursion with the telecom start-up, Confluent Photonics. At Draper, he focused on various MEMS sensors, optical waveguide devices, and electronic packaging technologies, optical waveguide biosensors, and atomic sensors including the chip scale atomic clock. He is currently the Group Leader of the Fabrication Processes Group for Draper's Microfabrication Facility. He has co-authored over 30 papers and one book chapter. He holds several patents.

Michael J. Tomaino-Iannucci was born in Danbury, Connecticut, in 1985. He received the B.S. degree in electrical engineering and physics from Tufts University in 2007 and the M.S. degree in applied physics from Yale University in 2009.

Since 2009, he has been with the Analog, Power, and Instrumentation Electronics Group, Draper Laboratory, Cambridge, MA, USA, and became a Senior Member of the Technical Staff in 2014. He has presented technical papers at several conferences and holds a patent in the field of nondestructive testing. His interests include low-noise and low-power electronics design, high-performance sensor development and testing, and innovative nondestructive testing methods and applications.

Jonathan S. Ung was born in Seattle, WA, USA, in 1993. He received the B.S. degree in mechanical engineering and the M.S.E. degree in mechanical engineering from Johns Hopkins University in 2015 and 2016, respectively. He was with Johns Hopkins University, where he focused on a project with the JHU Applied Physics Laboratory to integrate electronics into a satellite panel design. He was also worked in a research laboratory which aimed to characterize oil droplets in various wave conditions using digital holography.

Since 2016, he has been a Member of Technical Staff with the Sensors and Imaging Systems Group and the Precision Navigation and Timing Instrumentation Group, Draper Laboratory, Cambridge, MA, USA. His interests include finite-element analysis, mechanical design and testing of microelectromechanical systems sensors, and precision navigation sensors.

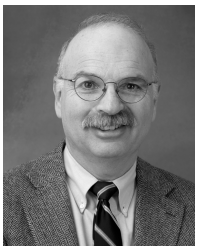

Marc S. Weinberg holds the B.S. and Ph.D. degrees in mechanical engineering from M.I.T., where he was an NSF Fellow. He co-invented the first useful silicon microelectromechanical systems gyro, which is now used in many applications. He holds 49 U.S. patents. His research on chemical sensors, balance prostheses, photovoltaics, and atomic clocks have led to start-ups or commercial applications. He is an AIAA Associate Fellow and a Professional Engineer.